Inorganic Chemistry

pubs.acs.org/IC

Article

Hybrid Materials Based on Keggin Phosphotungstate and Bipyridine with Valuable Hydrophobic and Redox Properties

Gabriel Hidalgo, Michel Devillers, and Eric M. Gaigneaux*

Cite This: *Inorg. Chem.* 2022, 61, 12494−12507

Read Online

ACCESS | Metrics & More | Article Recommendations | Supporting Information

ABSTRACT: A thorough investigation of two novel hybrid materials, namely, $(2,2'\text{-Hbpy})_3[PW_{12}O_{40}]$ and $(4,4'\text{-}H_2bpy)_{1.5}[PW_{12}O_{40}]\cdot 1.5H_2O$ built from Keggin phosphotungstic acid (PTA) and bipyridine, describes the impact of bipyridine isomers in their formation and physicochemical properties. The hybrids' formation was confirmed by powder X-ray diffraction, while infrared spectroscopy (IR) proved the polyoxometalate (POM) structural preservation. The stoichiometric composition and thermal stability of the hybrids were solved by thermogravimetric analysis−mass spectrometry, which also revealed newly acquired hydrophobic properties. Raman and IR spectroscopies demonstrated that the POM skeleton units in both hybrids were distorted compared to the POM in PTA, which induced a decrease of their reduction potentials as observed by diffuse reflectance ultraviolet−visible spectroscopy (DR−UV−vis). The hybrids' acidity was assessed by ammonia temperature-programmed desorption, which showed no remaining acid sites compared to the strong acidic character of the pristine PTA. The properties of the hybrids were tested in the epoxidation of cyclooctene in the presence of H_2O_2. The reaction was boosted when the hybrids were pre-activated with H_2O_2.

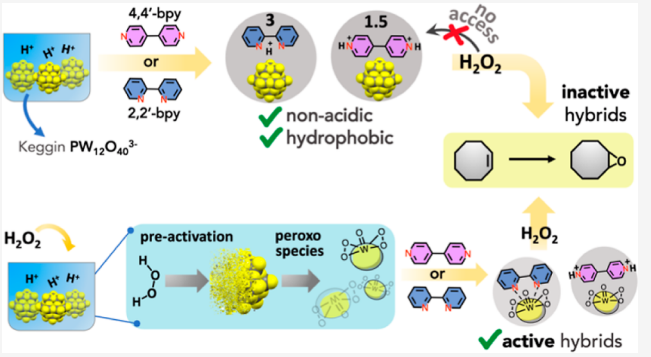

INTRODUCTION

Up until now, the extraordinary chemistry of polyoxometalates (POMs) has not gone unnoticed. Their versatile nature in terms of structure, size, and molecular properties appear to justify such attention.[1] Much of the interest in these compounds has emerged as a result of the impact of their practical use in many areas, such as materials science, physics, biology, chemistry, and catalysis.[2−6] The vast range of compounds falling into the POM category has permitted to split them into different groups. Heteropolyanions (HPAs), for example, have shown to be one of the most explored subsets of POM clusters with a large, and rapidly growing, number of publications and patents every year.[7] Most of these studies have focused on the Keggin $[XM_{12}O_{40}]^{n-}$ (mainly M = Mo or W and X = P, Si or Ge) HPA structure.[8] Derivatization of Keggin frameworks by exploitation of the POM anionic charge (ease of counterion exchange), and capacity to form lacunary structures (removal of cages atoms creating vacancies that can be filled by linker atoms) have enabled researchers to design different hybrid architectures in a reliable and predefined manner.[7,9] One of the common routes to integrate Keggin clusters into functional architectures lies on the preparation of organic−inorganic materials.[10] This includes, in particular, hybridization of Keggin HPAs with nitrogen-containing ligands. Formally, these organic−inorganic combinations are divided into two groups: Class I when the nature of the interaction of the components is relatively weak (*e.g.*, hydrogen bonding, van der Waals contacts, or electrostatic forces) and class II when the components exchange strong chemical bonds (*e.g.*, covalent, iono-covalent, or Lewis acid−base bonds).[11] The emerged new properties of these Keggin derivatives have been among others explored in catalysis. Illustrative examples are of three types. The first one comprises MOFs,[12−15] phase transfer,[16] and heterogeneous[17] models for oxidation reactions. The second type includes hybrids with Keggin entities in their protonated form (heteropoly acids).[18,19] This is typically achieved for acid−base reactions. Designs of the third type involve distinct types of lacunary HPAs and bipyridine for photocatalytic oxidation[20−23] and reduction[24] reactions. Exploration of hybrids made of Keggin HPAs and bipyridine has already been reported, although typically with bipyridine chelating transition metals,[25−29] few have been tested in catalytic oxidation reactions.[30] Other investigations, primarily in the area of materials science, have also combined metal-free bipyridine complexes with Keggin HPAs;[31−37] however, much of the emphasis has been focused on structural aspects from

Received: February 1, 2022
Published: August 4, 2022

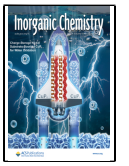

single-crystal X-ray diffraction measurements, rather than a careful examination of the effects of ligand isomerism and conformation, and of acidity factors that can strongly direct the final structure of the hybrid material. In fact, few, if any, systematic comparative studies on Keggin HPAs and isomers of bipyridine have been reported. More importantly, no convincing explanation has yet been proposed as to why and how isomers of this type do dictate the final stoichiometric composition and redox properties of the final hybrid material. In practice, the type of hybrid precursors and synthesis protocols commonly reported are used in an apparent arbitrary way. Addressing these remaining issues on systematic experimental basis would be advantageous, as it could provide new insights as to how the isomeric nature of the ligand affects the physicochemical properties of the hybrid material. Such understanding could be implemented in areas such as materials science and catalysis to produce useful hybrid materials of improved potential. Therefore, in the present study, we use the tungsten-based Keggin precursor phosphotungstic acid $H_3PW_{12}O_{40}$ (PTA), which has the highest thermal stability among the Keggin series, and typically shows the highest activities in catalytic oxidation reactions with H_2O_2.[5] In the latter case, H_2O_2 degrades the Keggin anion into lower nuclearity peroxo species such as $\{PO_4[WO(O_2)_2]_4\}^{3-}$ and $\{HPO_4[WO(O_2)_2]_2\}^{2-}$ anions.[38,39] The present work, therefore, deals with (i) a hydrothermal synthesis combining PTA and isomer 2,2′-bpy or 4,4′-bpy to, respectively, form $(2,2'\text{-Hbpy})_3[PW_{12}O_{40}]$ and $(4,4'\text{-H}_2\text{bpy})_{1.5}[PW_{12}O_{40}]\cdot 1.5H_2O$, (ii) a thorough spectroscopic comparison of the two hybrids highlighting their respective structural and bonding peculiarities and differences with respect to pristine PTA, and (iii) evaluation of the catalytic properties of the materials in the epoxidation of cyclooctene with H_2O_2. Herein, we disclose the potential of bipyridine ligands in the production of functional hybrid materials made of Keggin HPAs, and we rationalize the role of isomerism in the final stoichiometric composition of the material along with its redox and acid−base properties.

EXPERIMENTAL SECTION

Materials. 2,2′-Bipyridine (2,2′-bpy) (99%) and 4,4′-bipyridine (4,4′-bpy) (98%) from TCI chemicals; hydrochloric acid (HCl, 37 wt %) and hydrogen peroxide (H_2O_2, 30 wt %) from Carl Roth; cyclooctene (C_8H_{14}, 95%), dibutyl ether ($C_8H_{18}O$, 99%, stabilized with BHT), and acetonitrile (C_2H_3N, for HPLC, isocratic grade) from VWR chemicals, were purchased and used as received. PTA was purchased from Sigma-Aldrich in the form of $H_3PW_{12}O_{40}\cdot xH_2O$ (reagent grade). Before further use, the full powdered hydrated PTA was placed under vacuum (*ca.* 1.8×10^{-2} mbar) overnight at room temperature in order to evacuate all its physisorbed water and obtain the hexahydrate form $H_3[PW_{12}O_{40}]\cdot 6H_2O$.

Synthesis. *Synthesis of $(2,2'\text{-Hbpy})_3[PW_{12}O_{40}]$ (1) and $(4,4'\text{-H}_2\text{bpy})_{1.5}[PW_{12}O_{40}]\cdot 1.5H_2O$ (2).* To an aqueous mixture of PTA (1 mmol, 2.9881 g) in 9.5 mL of distilled water was added 2,2′-bpy (3 mmol, 0.4733 g, for **1**) or 4,4′-bpy (1.5 mmol, 0.2343 g, for **2**) and stirred (500 rpm) for 1 h at room temperature. The resulting suspension was transferred to a sealed stainless-steel autoclave (70 mL) equipped with a Teflon jacket and heated to 120 °C for 5 h and then cooled to room temperature. The resulting white precipitate was filtered, rinsed several times with distilled water, and dried overnight under vacuum (*ca.* 1.8×10^{-2} mbar) at room temperature.

Synthesis of compounds 3 and 4. Compounds **3** and **4** were prepared with the idea to probe the effect of pre-activation of PTA with H_2O_2 on the hybridization. To an aqueous solution of H_2O_2 (10.21 mL, 100 mmol) was therefore first added 2.9881 g (1 mmol) of PTA and stirred (500 rpm) for 1 h at room temperature. Subsequently, as was done for **1** and **2**, 0.4733 g of 2,2′-bpy (3 mmol, for **3**) or 0.2343 g of 4,4′-bpy (1.5 mmol, for **4**) was added and stirred (500 rpm) for 1 h. The resulting white precipitate was filtered, rinsed several times with water, and dried overnight under vacuum at room temperature.

Synthesis of Bipyridinium Salts. With the objective to probe the protonation state of bipy ligands in the hybrids, fully protonated salts of 2,2′-bipyridine (2,2′-bpy) (99%) and 4,4′-bipyridine (4,4′-bpy) were prepared as reference materials. To an aqueous solution of HCl (7.91 mL, 0.2 mol·L^{-1}) was added 0.0473 g of 2,2′-bpy (0.3 mmol) or 0.0469 g of 4,4′-bpy (0.3 mmol) and stirred (500 rpm) for 1 h. The obtained solution was dried under vacuum (*ca.* 1.8×10^{-2} mbar) overnight at room temperature. The light pink or white colored powder obtained for precursor 2,2′-bpy or 4,4′-bpy, respectively, was later stored in a desiccator for further characterization.

Characterization of Samples. Powder X-ray diffraction (PXRD) patterns were recorded at room temperature on a Bruker-D8 advance diffractometer (Bragg−Brentano geometry), equipped with a LYNXEYE XE-T detector, using Cu Kα radiation (λ = 0.15418 nm). The X-ray source was operated with a tension of 40 kV and a current of 30 mA. Diffractograms were collected between 5 and 80° (2θ) and rotated to 5 rpm with a 0.015° increment and 0.15 s per integration step.

Fourier transform infrared spectra (IR) were recorded on a Bruker Equinox 55 with a DTGS detector equipped with a Bruker ATR platinum cell with diamond crystal. The spectra were obtained by recording 500 scans from 400 to 4000 cm^{-1} with 20 cm^{-1} resolution in transmittance mode and analyzed by the software OPUS.

Diffuse reflectance ultraviolet−visible spectroscopy (DR−UV−vis) was carried out in a Shimadzu UV-3600 plus apparatus equipped with a Harrick Praying Mantis diffuse reflection accessory. The background of the samples was referenced to a $BaSO_4$ pellet material and recorded from 600 to 190 nm wavelength range with a sampling interval of 0.5 nm and a slit width of 2 nm. The reflectance values were automatically transformed to Kubelka−Munk with the integrated software UVProbe 2.62.

Raman spectra were recorded on a Bruker spectrometer (type RFS100/S) equipped with a liquid nitrogen detector and a Nd:YAG laser supplying the excitation line at 1064 nm with a power of 100 mW. The spectra were collected recording 32 scans in the range of 400−4000 cm^{-1} at 4 cm^{-1} resolution and analyzed with OPUS software.

Thermogravimetric analysis−mass spectrometry (TGA−MS) was performed in a Mettler Toledo TGA/DSC 3+ apparatus coupled with a Pfeiffer Vacuum ThermoStar mass spectrometer. The samples were initially stabilized at 25 °C during 15 min and subsequently heated from 25 to 900 °C at 10 °C/min under a synthetic air flow (50 mL/min, 80% N_2 and 20% O_2 Alphagaz 1 Air Liquide).

Ammonia temperature programmed desorption (TPD-NH_3) was performed in a Hiden CATLAB combined microreactor and mass spectrometer (MS) system (MS being equipped with a quadrupole). The experiments were performed according to the following five steps: (i) the sample was pre-heated from room temperature to 100 °C at 10 °C/min for 2 h under a synthetic air flow (50 mL/min, 80% N_2 and 20% O_2 Alphagaz 1 Air Liquide); (ii) under an Ar flow (50 mL/min, Alphagaz 1 Air Liquide), the temperature decreased from 100 to 50 °C at 10 °C/min; (iii) adsorption of NH_3 (5% in He, Mixture Crystal Air Liquide) flow (20 mL/min) mixed with a flow of Ar (30 mL/min) at 50 °C during 30 min; (iv) flush, at 50 °C, of pure Ar (50 mL/min) for 2.5 h; (v) heating from 50 to 800 °C under Ar (50 mL/min) at 10 °C/min.

The weight percentages of W and P were measured by inductively coupled plasma−atomic emission spectroscopy on an ICAP 6500 Thermo Scientific equipment. The samples were calcined at 500 °C and subsequently decomposed by addition of sodium peroxide. Elemental analysis for C and N was performed using an Elementar, L-Cube equipment.

^{1}H NMR spectra were recorded at room temperature (295 K) on a Bruker Avance 500 operating at 11.7 T (Larmor frequency of 500

https://doi.org/10.1021/acs.inorgchem.2c00342
Inorg. Chem. 2022, 61, 12494−12507

Scheme 1. Synthesis Illustration of Compounds 1 and 2 from PTA and Bipyridine Isomer Precursors

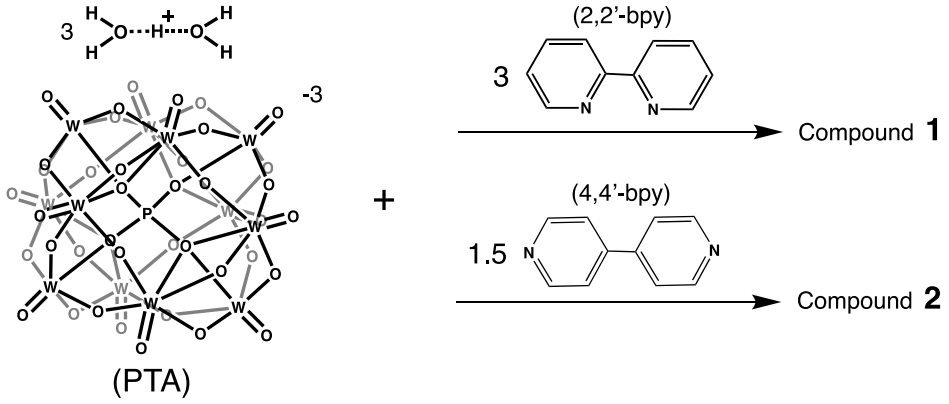

MHz). Experiments were run under the TopSpin program (Bruker) using a BBO{^{1}H,X} probehead equipped with a *z*-gradient coil.

Catalytic Experiments. The catalytic tests were carried out at 70 °C under air in a closed 10 mL round-bottomed two-neck flask reactor equipped with a reflux condenser, oil bath, and magnetic stirring rod (500 rpm). Typically, the reactor was loaded with catalyst (mass adjusted to 0.02 mmol of W atoms in the reactor); solvent CH_3CN (9.59 mL); internal standard dibutyl ether (1 mmol); 30 wt % aq H_2O_2 (1 mmol); and cyclooctene (1 mmol). Before olefin addition, the reaction was pre-heated at the desired reaction temperature, and the reaction time was counted immediately after olefin addition. The catalytic reaction was monitored every hour using a Shimadzu GC-2010 PLUS equipped with a capillary column (Shimadzu SH-Rtx-1 15 m × 0.25 mm) and a flame ionization detector. Assignments of reagents and products were made by comparison with authentic samples. Hot filtration tests, to explore the eventual occurrence of leaching of active species from the solids to the reaction liquid medium, were carried out under typical catalytic conditions for 2 h after which the solid was separated from the reaction medium by filtration with a syringe equipped with a 0.2 μm VWR membrane filter. The remaining solution was subsequently monitored by gas chromatography (GC), at 70 °C.

RESULTS AND DISCUSSION

Synthesis and Stoichiometric Compositions of 1 and 2. Compounds **1** and **2** were hydrothermally synthesized *via* a stoichiometric counter-cation exchange. Quantities were based on the measured pH (pH = 0.63) of the PTA solution and theoretical pK_a values (see values *infra*) of the protonated bipyridine ligands. As illustrated in Scheme 1, the molar ratio ligand/POM was kept at 3/1 for **1** and 1.5/1 for **2** in order to balance the three times negatively charged POM anion with positively charged ligands and meet the charge equivalence (vide infra).

In order to confirm the formation of the compounds, the samples were examined by PXRD and compared with their respective precursors. Figure 1a,b displays newly formed crystalline phases that emerged from their constituent units confirming the compounds' construction. The absence of peaks of the precursors and the appearance of new peaks reflect the great purity of the compounds. The compounds show well-defined diffraction peaks that differ from each other as a result of the different modes of molecular packaging adopted by the ionic building units after hybridization (Figure 1c).

TGA−MS was used to evaluate the stoichiometric composition and thermal stability of the compounds. The thermogravimetric profile of PTA shows three events (Figure 2). The first two mass losses at 74 °C (0.5%) and 190 °C

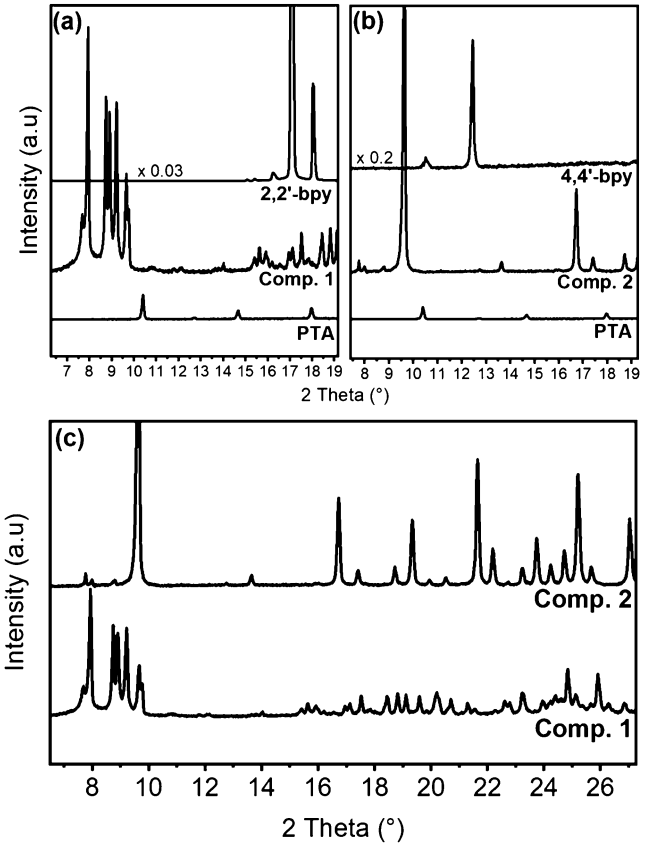

Figure 1. PXRD patterns where (a,b) refer to compounds **1** and **2** with their respective precursors; and (c) compares the two compounds.

(3.7%) correspond to the departure of physisorbed and crystalline water, the latter occurs due to the breakdown of the symmetrical adduct $H_2O\cdots H^+\cdots OH_2$.[40] The third loss (0.9%) at 466 °C accounts for the release of acidic protons in the form of H_2O, and the beginning of decomposition of the Keggin structure.[5]

Unlike PTA, the thermal profile of **1** consists in two steps at higher temperatures. The first (5.2%) and second (9.4%) mass losses at 456 and 556 °C, respectively, were identified as departures of mixtures of water and CO_2 as a result of the oxidative decomposition of bipyridine. Although **1** does not show a thermal event related to the departure of physisorbed or crystalline water, the observed water loss is assumed to

https://doi.org/10.1021/acs.inorgchem.2c00342
Inorg. Chem. 2022, 61, 12494−12507

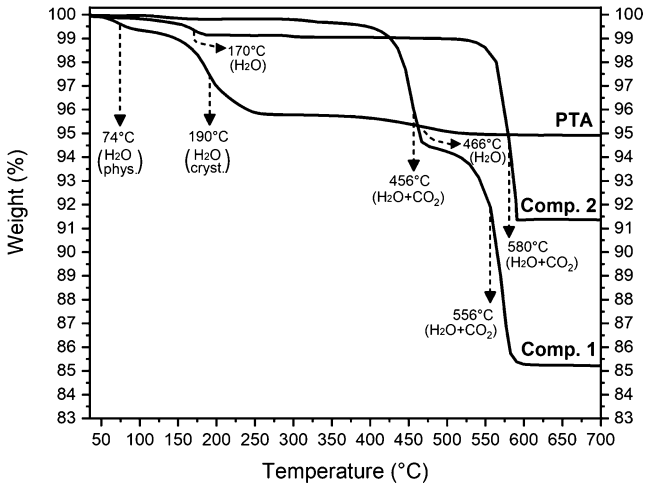

Figure 2. TGA−MS profiles of compounds **1**, **2**, and PTA precursor (under air, 10 °C/min).

derive from the reaction between protons of bipyridinium (2,2′-bpyH$^+$) and POM peripherical oxygens. The moles of POM and bipyridine were determined based on the known total mass of the sample, the mass fraction of the burned ligand, and the residual inorganic content. The latter corresponds to the POM fraction that is thermally decomposed to WO_3 and P_2O_5 simple oxides after heating above 600 °C.[41] Consequently, the stoichiometric ratio of ligand/POM was determined as 3/1 and corresponds to $(2,2'\text{-Hbpy})_3[PW_{12}O_{40}]$. Compound **2**, on the other hand, displays a different thermal profile. In a single step (8.2%), the ligand and water were released at 580 °C. However, an additional mass loss (0.7%) at 170 °C identified by MS as water, presumably the crystallization one, was detected. The stoichiometric ratio ligand/POM was therefore calculated as 1.5/1 and corresponds to $(4,4'\text{-}H_2bpy)_{1.5}[PW_{12}O_{40}]\cdot 1.5H_2O$. The stoichiometric composition of the compounds suggests that the structural inclusion of crystalline water in **2** was caused by the low number of hydrophobic bipyridine ligands per hydrophilic POM unit, while the number of ligands in **1** appears to be high enough for bipyridine to fully expel structural water, making **1** more hydrophobic than **2**. Elemental analysis (Table 1) confirms that **1** is composed of 1 POM (W/P = 13, which is close to the expected value of 12) and 3 bipyridines (*i.e.*, 12W/6N = 2) and that compound **2** is made of 1 POM (W/P = 12) and 1.5 bipyridine (*i.e.*, 12W/3N = 4). The calculated stoichiometry of **1** and **2** shows good agreement with the intrinsic basicity of the ligands. Bipyridine in acidic media undergoes protonation in two steps giving rise to monoprotonated $[bpyH]^+$ and diprotonated $[bpyH_2]^{2+}$ species.[42] Depending on how the two pyridine rings are connected (*i.e.*, through 2,2′ or 4,4′ carbon atoms), the protonation process is less or more restricted. Considering that the dissociation constants of 2,2′-bpyH$_2^{2+}$ (pK_{a1} = −0.2 and pK_{a2} = 4.4) are substantially lower than 4,4′-bpyH$_2^{2+}$ (pK_{a1} = 2.5 and pK_{a2} = 4.9),[43] the 4,4′-bpy isomer undergoes double protonation much easier than 2,2′-bpy whose double protonation requires very strong acidic conditions. Notice that under our synthesis conditions, the solid ligands were added to an aqueous solution of PTA at pH = 0.63, which is sufficiently acidic to doubly protonate 4,4′-bpy but 2,2′-bpy only once.[43,44] Hence, the calculated stoichiometric composition of the compounds appears consistent with the difference of diffraction patterns observed in Figure 1c, namely, the distinct number of ligands per POM unit in the respective hybrids, likely caused them to organize differently.

Protonation and Conformation of Hybridized Ligands. To verify the protonated state of the ligands after hybridization, the compounds were examined by IR and Raman spectroscopy techniques and compared with the prepared fully protonated bipyridinium salts of each isomer. In the mid-frequency region of Figure 3a (*ca.* 1600 cm^{-1}), the

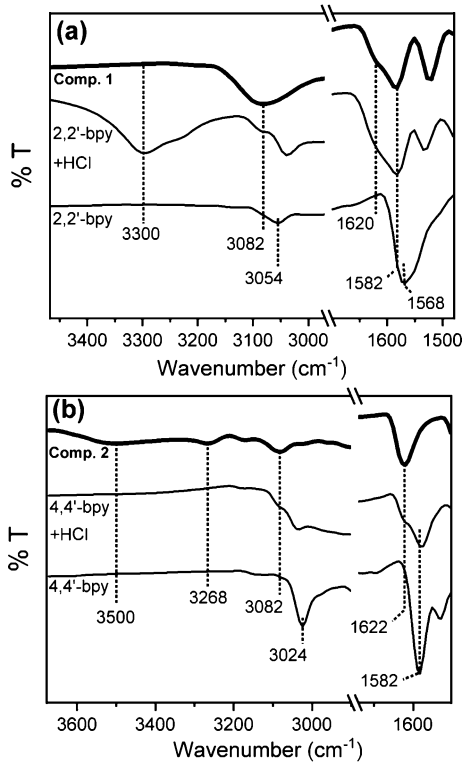

Figure 3. IR spectra of **1** (a) and **2** (b) in the mid- and high-frequency regions.

ring stretching of 2,2′-bpy appears at 1568 cm^{-1}.[45] This band is blue-shifted to 1582 cm^{-1} for the protonated ligand with an additional shoulder at 1620 cm^{-1} due to the N−H bending.[46] This is similar as what is observed for **1**.

In the high-frequency region (above 3000 cm^{-1}), the stretching N−H mode at 3300 cm^{-1} of the protonated ligand

Table 1. Elemental Analysis

compound	W (wt %)	P (wt %)	C (wt %)	N (wt %)	W/P (mol)	W/N (mol/mol)
1	74.3	0.9	12.8	2.8	13	2
2	74.1	1.0	6.3	1.5	12	4
3	42.4	0.1	28.0	6.4	52	0.5
4	49.9	0.1	16.5	3.8	120	1

https://doi.org/10.1021/acs.inorgchem.2c00342
Inorg. Chem. 2022, 61, 12494−12507

appears absent in **1**; rather a wide blue-shifted band centered at 3082 cm^{-1} in the C−H stretching region is observed.[47] As **1** is supposed to be protonated, one could expect the appearance of the stretching N−H mode. One possible explanation for this is that the protonated bipyridine in **1** is positioned or interacting with the POM in such a way that the stretching N−H vibrational mode is constrained by symmetry, preventing its manifestation in IR. On the other hand, in the mid-frequency region of Figure 3b, **2** displays a single blue-shifted band at 1620 cm^{-1} (relative to the neutral 4,4′-bpy) without a shoulder as shown by the protonated 4,4′-bpy. In the high-frequency region, three small bands appear and were tentatively assigned as stretching bands of C−H at 3082 cm^{-1}, N−H at 3268 cm^{-1}, and O−H at 3500 cm^{-1}.[40,47] Therefore, the obtained vibrational lines clearly indicate that the ligands are protonated inside the compounds, and, in addition, the observed vibration of O−H groups reinforces the data obtained by TGA showing that **2** is hydrated.

Raman spectroscopy was used to examine the protonated conformation of the hybridized ligands and the corresponding bipyridinium salts. The spectra were recorded in the mid-frequency region where two key vibrational modes are discussed (Figure 4). In Figure 4a, the neutral 2,2′-bpy shows bands of ring stretching at 1591 and 1573 cm^{-1} and C−H bending at 1301 cm^{-1}.[48] Since the two bounded pyridine rings in 2,2′-bpy are neutral, bands of ring stretching below 1600 cm^{-1} and C−H bending at ∼1300 cm^{-1} are expected.[43]

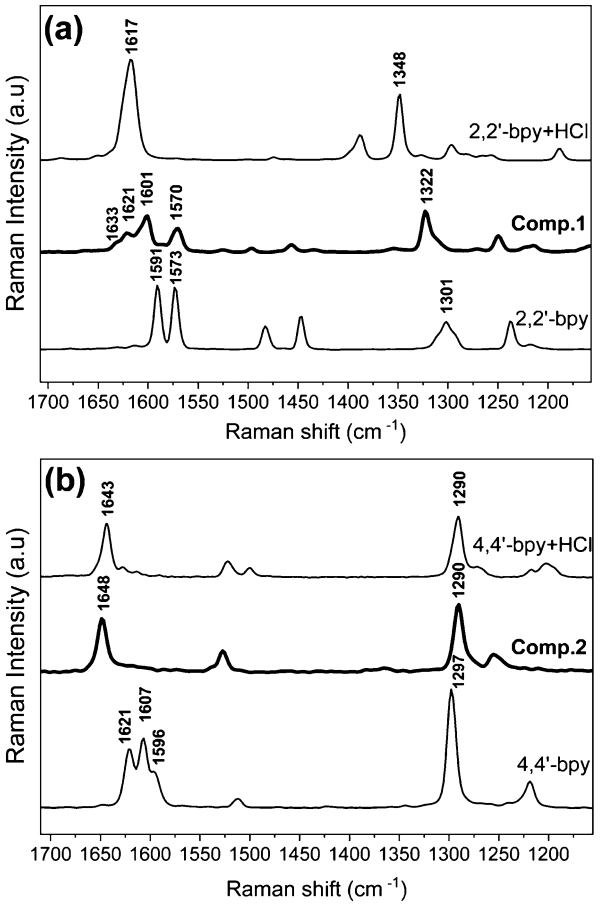

Figure 4. Raman spectra of **1** (a) and **2** (b) with their respective neutral and protonated ligand precursors in the mid-frequency region.

The protonated 2,2′-bpy salt, on the other hand, shows that these bands blue-shifted at 1617 and 1348 cm^{-1}, indicating the presence of two pyridinium rings vibrating above 1600 cm^{-1} with a large blue-shifted bending C−H band. Therefore, the prepared bipyridinium salt appears as a diprotonated *trans*-2,2′-bpyH_2^{2+} species. Since the spectrum of **1** shows a combination of stretching bands of pyridinium at 1633, 1621, 1601, and pyridine at 1570 cm^{-1}, accompanied by a less shifted band at 1332 cm^{-1} relative to the protonated salt, the ligand species in **1** were therefore identified as a monoprotonated *cis*-2,2′-bpyH^+ species. Along the same line, the spectra of **2** and of the protonated 4,4′-bpy salt (Figure 4b) were straightforwardly assigned to the diprotonated 4,4′-bpyH_2^{2+} species. The conformation assignments show reasonable agreement with previous examinations of protonated bipyridines in zeolites[43] and electrode surfaces,[49] and further support the stoichiometric calculations established from TGA (Figure 2).

Effect of Hybridization on POM Structure. To verify the POM integrity after hybridization, the characteristic vibrational fingerprints of the POM skeleton unit were studied in the infrared low-frequency region (Figure 5). PTA displays

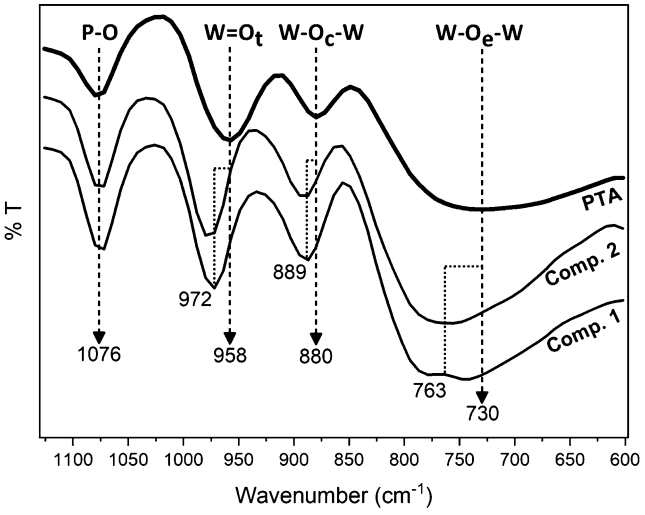

Figure 5. IR spectra showing the POM skeletal vibrations of **1**, **2**, and PTA in the low-frequency region.

typical bands of phosphorus-bound oxygen (P−O_a) at 1076 cm^{-1}, tungsten terminal oxygen (W═O_t) at 958 cm^{-1}, tungsten oxygen corner-sharing (W−O_c−W) at 880 cm^{-1}, and tungsten oxygen edge-sharing (W−O_e−W) bond at 730 cm^{-1}.[50,51]

Collected spectra reveal that after hybridization, the POM structure was retained in both compounds. In addition, except for the P−O_a band, all bands of hybridized POMs appear blue-shifted relative to PTA. A plausible interpretation of these vibrational displacements is based on the assumption that the hybridized POMs are no longer effectively participating in a hydrogen bond event such as POM and adduct $H_5O_2^+$ in hexahydrate PTA[40] (Scheme 1). In the latter, the oxygen−tungsten bonds in the POM outer sphere (*i.e.*, shared O−W−O, and W═O_t) elongate when they form an effective (the O···H distance is usually less than the sum of their van der Waals radii, and with a linear angle close to 180°) hydrogen bond with the adduct $H_5O_2^+$ (*e.g.*, W═O···$H_5O_2^+$). In the case of **1** and **2**, likely the electrostatic interactions between POM and

https://doi.org/10.1021/acs.inorgchem.2c00342
Inorg. Chem. 2022, 61, 12494−12507

bipyridinium (O···Hbpy$^+$) in the packing network do not allow an effective hydrogen bond interaction, and therefore, the hybridized W═O_t and shared W−O−W oxygen bonds are not elongated as in the case of PTA, leading to an increase in vibrational frequency.[52] Complementary Raman spectroscopy was employed to examine the symmetry bands associated with the POM terminal W═O_t. As Raman vibrational modes are determined by symmetry and bonding of molecular species,[53] alteration of the W═O_t molecular environment is expected to affect the position of the Raman bands.

PTA displays an intense band at 1004 cm^{-1} accompanied with a small band at 998 cm^{-1} attributed to the symmetric and antisymmetric stretching of W═O_t, respectively[50] (Figure 6).

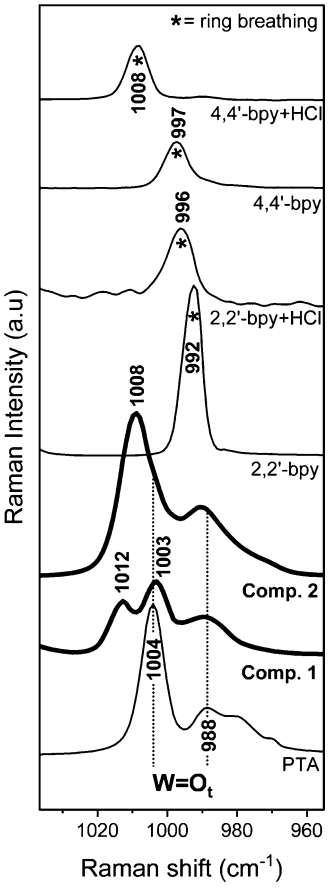

Figure 6. Raman spectra of **1**, **2**, and PTA showing terminal W═O_t and ring breathing bands of 2,2′-/4,4′-bpy in the low-frequency region.

Likewise, in this region, bipyridine also displays a ring breathing band that is blue-shifted upon protonation.[43] As a result, the compounds targeting symmetric W═O_t stretching band appear overlapped. The symmetric stretching band W═O_t of **1** may, for example, be the band at 1012 or 1003 cm^{-1}, or it could be hidden in-between both bands. For this reason, we only discuss the antisymmetric W═O_t band of the compounds whose region is not masked by bands of protonated ligands and therefore allows for unambiguous interpretation of the spectra. The antisymmetric W═O_t band appears blue-shifted markedly in **2** and to a lesser degree in **1** relative to PTA. Previous studies that correlate Raman frequencies with metal oxide bond distances[53] allow claiming that the observed Raman shifts were caused by distortion of the POM octahedral WO_6 units relative to those in PTA. It appears, therefore, that a shift to higher frequencies leads to a greater (less regular) distortion of the octahedral WO_6 units that build the POM. This distortion, presumably caused by the counter cationic exchange with bipyridine, made the overall structure of the hybridized POMs less regular than the POM in PTA, following an increase of irregularity in the order PTA < **1** < **2**. This view is supported by the infrared vibrational displacements (shortened W−O bonds) previously observed (Figure 5).

The electronic properties of the compounds and PTA were analyzed by DR−UV−vis. In order to relate DR to sample absorption and therefore obtain sharper lines, the DR spectra were converted to Kubelka−Munk function $F(R_\infty)$ *versus* wavelength curves. Figure 7 shows absorption peaks in the range of 200−400 nm due to the ligand−metal charge transfer (LMCT) $O^{2-} \rightarrow W^{6+}$ of the WO_6 octahedral units that assemble the POM.[54,55]

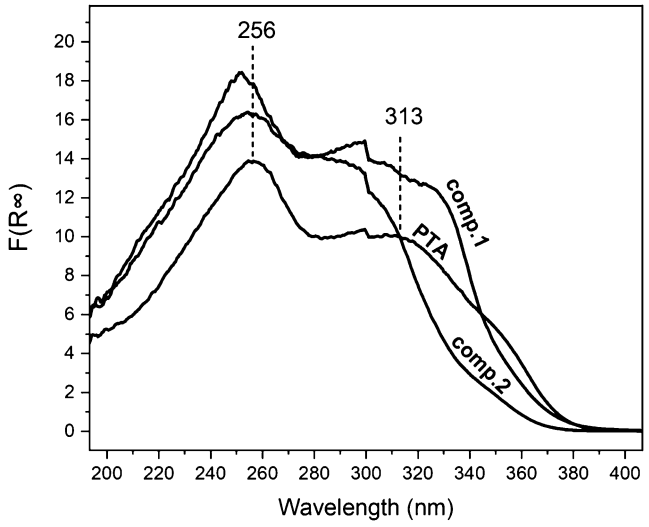

Figure 7. Kubelka−Munk function *vs* wavelength of **1**, **2**, and PTA at room temperature in the UV region.

PTA displays two main absorption bands centered at 256 and 313 nm, values which appear blue-shifted in the absorption profile of the compounds, except for the red-shifted band of **1** with respect to the 313 nm band of PTA. Earlier examinations by DR−UV−vis[56,57] indicate that not only one, but multiple factors influence the shape and position of absorption bands of POMs and metal oxide clusters. These include local and overall symmetry, anion size, counter-cation polarizing effect, counter-cation size, and interaction between anions. In our case however, those factors are minimized since our three samples display structural similarities. For instance, modification of the local (WO_6 octahedra) and overall (POM structure) symmetries can be discarded as origin of the observed shifts as they are the same for all the samples, although slightly distorted in the hybrids as previously seen in Raman (Figure 6). The influence of the POM size is excluded as well since the samples share the same anion. The polarizing effect, which increases for small and highly charged cations, is expected to broaden the lowest energy transition band (*ca.* 280−380 nm) to higher wavelength. This red-shift broadening should therefore increase in the following sequence: **1** < **2** < PTA, and not **2** < PTA < **1** as in our case, and thus, this effect could be ignored. The same absorption tendency should be observed

https://doi.org/10.1021/acs.inorgchem.2c00342
Inorg. Chem. 2022, 61, 12494−12507

when the counter-cation size decreases in the following order: **2** ≈ **1** < PTA, and not **2** < PTA < **1**. It thus appears that the major factor affecting the charge transfer energy derives principally from the separation or interaction between POM units, which can be studied by calculating the band gap energy (E_g) from the UV absorption spectra of Figure 7.

In order to estimate E_g values from the Kubelka–Mulk plot, the Tauc's relation $[F(R_\infty)h\nu]^{1/2}$ *versus* photon energy[58] was plotted. The values were determined by finding the energy intercept of a straight line drawn tangent to the inflection point of the curves[59] (Figure 8). The obtained E_g values are regarded

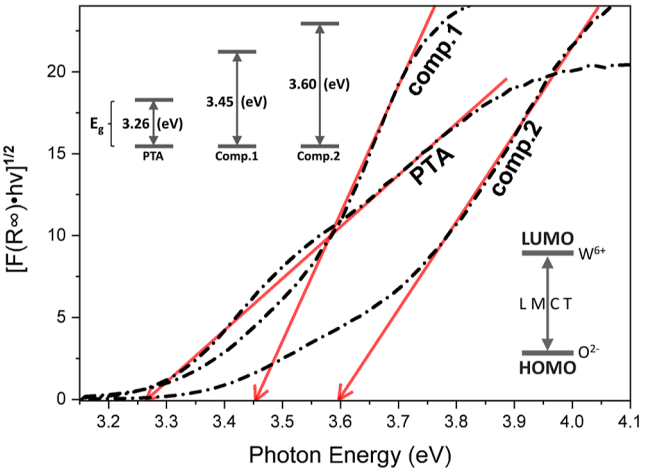

Figure 8. Band gap (E_g) energy values determined from Tauc's relation $[F(R_\infty)h\nu]^{1/2}$ *vs* photon energy for **1**, **2**, and PTA.

as the amount of energy needed to promote electrons from POM oxygens (acting as ligands) to tungsten atoms upon irradiation creating a LMCT process.[60] Specifically, this corresponds to a transfer of electron density from the highest occupied molecular orbital (mainly from the lone pair electrons on bridging oxygen sites) to the lowest unoccupied molecular orbital (mainly localized on the W atoms).[61] The Tauc plot displays PTA with the smallest band gap value (highest reduction potential[62]), followed by **1** and **2**. Earlier DR–UV–vis POM studies have reported direct connections between E_g values and POM distances when POMs are thermally pre-treated or supported.[62−65] Generally speaking, POMs showed a decrease in E_g when increasing the degree of dehydration (compacting of the structure by removal of crystalline water) and an increase in E_g when spreading on supports or when separated from one another by voluminous counter cations. It appears, therefore, that when POM units are closer in distance, they act as a larger POM inducing an E_g diminution and the opposite when separated, this being the most significant factor affecting the E_g energy. To summarize, the obtained E_g values from Figure 8 likely indicate that after hybridization the distances between POM anions increased, inducing an E_g augmentation due to isolation and less interaction between the POM units.

Influence of Hybridization on the Acid Properties of PTA. In view of the practical use of the compounds in epoxidation catalysis (where presence of acid sites has to be avoided as they hydrolyze the desired epoxide product, resulting in lower selectivities), the samples were subjected to NH_3-TPD analysis, in order to assess the presence and strength of accessible acid sites potentially remaining within the compounds. Figure 9 displays weak, medium, and strong site segments. The curve of PTA shows weak and strong acid

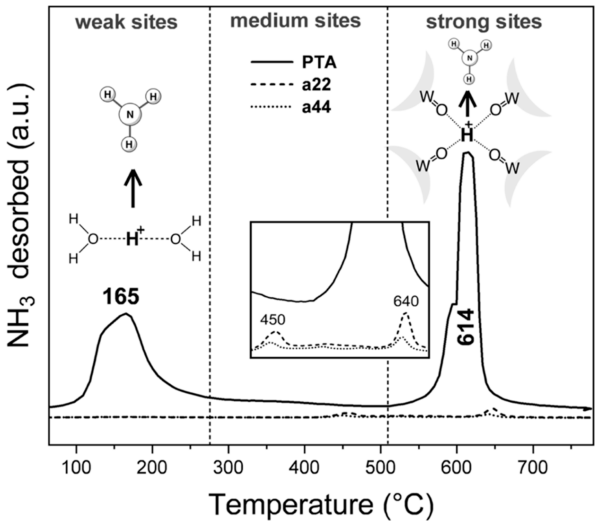

Figure 9. NH_3 thermodesorption of PTA, **1**, and **2** (10 °C/min under air; initial pre-heating of 2 h at 100 °C). The inset plot depicts a zoom view of **1** and **2**.

sites at 165 and 614 °C, respectively. The first asymmetric peak is attributed to weakly adsorbed NH_3. This desorption event appears in the interval of 100–270 °C, where under the same heating rate, the thermal departure of crystalline water was observed in TGA (Figure 2). Therefore, the desorbed peak centered at 165 °C likely corresponds to a labile N···H^+ interaction between NH_3 and hydrated Brønsted $H_2O\cdots H^+\cdots OH_2$ sites ($H_5O_2^+$ adduct). The observed peak asymmetry is presumably associated with a two-step rupture of the adduct, which disappears gradually upon dehydration.[40] In the strong acid segment (557–660 °C), the second asymmetric desorption peak appears centered at 614 °C. In this temperature range, W═O···H^+···O═W proton species migrate between four POM units,[66] and likely correspond to NH_3 strongly held as NH_4^+ species whose desorption was simultaneously accompanied by degassing of N_2 (m/z = 28), H_2 (m/z = 2), and H_2O (m/z = 18 and 17) according to the m/z signals obtained from the mass spectrometer. These products have been reported as a result of a series of parallel events involving thermal or catalytic decomposition of $(NH_4)_3PW_{12}O_{40}$ (from NH_3 + $H_3PW_{12}O_{40}$) producing NH_3 + $H_3PW_{12}O_{40}$, decomposition of NH_3 to N_2 + H_2, and reduction of PTA by H_2 producing H_2O + $H_3PW_{12}O_{40(reduced)}$.[67,68] The compounds, on the other hand, display two very small desorption peaks centered at 450 and 640 °C, revealing a negligible acidity relative to the strong acid PTA. A tentative explanation of the poor desorption shown by the compounds may be proposed from an acid–base or hydrogen bonding point of view. In the former view, the NH_3 probe (pK_a = 9.3 for NH_4^+[69]) considered as a stronger base than bipyridine (pK_{a2} = 4.4 for 2,2′-bpyH$^+$, and pK_{a1} = 2.5 for 4,4′-bpyH$_2^{2+}$[43]) could interact with the protons held by bipyridine (forming bipyridinium) and thereby generate adsorption, which appears not to be the case. On the other hand, the hydrogen bonding view considers these protons as unavailable species (*i.e.*, no longer acidic) since they form stable intramolecular N^+–H hydrogen bonds with bipyridine and at the same time, they interact intermolecularly with the

https://doi.org/10.1021/acs.inorgchem.2c00342
Inorg. Chem. 2022, 61, 12494−12507

skeleton network of the POMs (N^+−H···O═W interactions). The latter view is consistent with our spectroscopic evidence that proved the protonation and electrostatic interactions of ligand−POM, and TGA which showed that the interactions were such that the ligands had to thermally decompose above 500 °C in order to detach from the POM structure. In summary, one of the effects of hybridizing PTA appears to result in the loss of its high acidity by protonating the ligands and forming the final neutral hybrid salt, thus stabilizing the overall structure through hydrogen bonding interactions. Finally, based on the thermodesorption measurements, the compounds were catalytically tested in the epoxidation of cyclooctene, as lack of acid sites promises the prevention of hydrolysis of the target epoxide.

Catalytic Epoxidation of Cyclooctene with H_2O_2. The catalytic performances of **1** and **2** were explored in the epoxidation of cyclooctene with H_2O_2 as the co-oxidant. The compounds showed poor activity when H_2O_2 and olefin were introduced after loading the catalyst, solvent, and internal standard, and preheating the reaction mixture to 70 °C (entries 1 and 5 of Table 2), similar to the 5% conversion observed without the catalyst. A modest improvement in conversion was noticed when the compounds were exposed 1 h to H_2O_2 (denoted as "exposed compounds") prior olefin addition (entries 2 and 6 of Table 2). The diffractograms of fresh and exposed compounds (Figure S1) revealed that the crystalline structures of the exposed compounds were not significantly altered. Only for exposed **1**, additional diffraction peaks (at 8.41 and 9.97°) were detected. These may correspond to small fragments of unknown active intermediate species that formed during the exposure to H_2O_2, and probably contributed to the slightly superior catalytic activity shown by exposed **1** compared to exposed **2**. IR, on the other hand, showed no variation in the vibrational modes between exposed and fresh compounds (Figure S2), indicating that H_2O_2 did not disturb the POM skeleton of the exposed compounds, in line with the structural preservation observed by PXRD. Based on the fact that hybridization appears to protect the hybridized POMs against degradation and knowing that, on the other hand, H_2O_2 requires direct access to the POM structure in order to produce active species,[70] a pre-activation strategy was conducted, namely, exposing the POM to H_2O_2 at the level of the preparation of the hybrids.

Table 2. Comparison of Different Catalytic Strategies of Compounds and PTA in the Epoxidation of Cyclooctene (COO)[a]

entry	sample	conversion (%)	COO selectivity (%)
1	**1**/H_2O_2/cyclooctene	10	100
2	(**1**/H_2O_2)1 h/cyclooctene	17	100
3	**3**/H_2O_2/cyclooctene	50	100
4	**3**/H_2O_2/cyclooctene[b]	73	100
5	**2**/H_2O_2/cyclooctene	7	100
6	(**2**/H_2O_2)1 h/cyclooctene	9	100
7	**4**/H_2O_2/cyclooctene	21	100
8	**4**/H_2O_2/cyclooctene[b]	71	100
9	PTA/H_2O_2/cyclooctene	10	
10	(PTA/H_2O_2)1 min/cyclooctene	69	92
11	PTA/cyclooctene/H_2O_2[b]	93	4

[a]Reaction conditions: catalyst (0.02 mmol of W), H_2O_2 (1 mmol), cyclooctene (1 mmol), 70 °C, 8 h. [b]Reaction conditions: catalyst (0.4 mmol of W), H_2O_2 (1 mmol), cyclooctene (1 mmol), 70 °C, 8 h.

Precisely, addition of an excess of H_2O_2 to the aqueous solution containing PTA was done prior to the addition of the bipyridine ligand. The collected powders were labeled as compounds **3** (when employing 2,2′-bpy) and **4** (using 4,4′-bpy). Comparison of the diffractograms between pre-activated (**3** and **4**) and non-activated (**1** and **2**) samples showed that the pre-activation process caused a radical change in the crystalline structure of the pre-activated compounds as different crystalline phases relative to **1** and **2** were observed (Figure 10a). The pre-activation strategy showed to have a beneficial effect on the catalytic activity (entries 3 and 7 of Table 2), as significantly higher conversion values were observed compared to their non-activated counterparts. Hot filtration tests (Figure S3) carried out for **3** and **4**, however, showed that the improved catalytic activity occurs mainly in the homogeneous phase as activity was detected after the filtration of the solid catalysts. In addition, the filtrated mixtures of **3** and **4** after a 24 h batch run were evaporated to dryness, and the recovered solids were analyzed by Raman spectroscopy (Figure S4). In the mid- and low-frequency regions, the bands of the resultant recovered solids closely matched those of fresh **3** or **4** accordingly. These bands were also accompanied by additional vibrational bands of adsorbed components of the reaction mixture (based on the vibration of $-CH_3$ groups at 2928 and 2861 cm^{-1}).

Hence, this demonstrates that the homogeneous active epoxidation species are hybrid compounds (*i.e.*, **3** or **4**) that were dissolved in the reaction mixture. In order to compare the effects of hybridization, the unhybridized and completely soluble PTA precursor was tested in the epoxidation. When H_2O_2 and olefin were immediately added after loading PTA, poor conversion and no epoxide production was observed (entry 9 of Table 2). Nevertheless, when the experiment was carried out but introducing the olefin after having allowed PTA to react 1 min with H_2O_2, conversion and selectivity improved dramatically (traces of 1,2-cyclooctanediol and other unidentified by-products were also detected by GC) (entry 10 of Table 2). As displayed in Figure 11, the conversion of PTA appears to be determined by the H_2O_2 exposure period, showing almost constant conversion values from 1.5 to 24 h. Conversely, within the first 8 h, the pre-activated compound **3** displayed inferior but growing activity that even surpassed that of PTA after 24 h.

The high PTA selectivity was later clarified when amounts of **3**, **4**, and PTA were increased 20-fold. A constant 100% selectivity and improved conversion were observed for **3** and **4** (entries 4 and 8 of Table 2), contrary to the drastic decrease in selectivity shown by PTA (entry 11 of Table 2). Therefore, the affected selectivity proved that at low concentrations (*i.e.*, 0.002 (mol W)/L), the acidity of PTA in the catalytic mixture is negligible and thus unable to hydrolyze the epoxide until PTA loading is increased. To summarize, the catalytic experiments demonstrated that the epoxidation of cyclooctene by PTA is restricted by the exposure period with H_2O_2 and detrimental for the epoxide when increasing catalyst loading. Conversely, the catalytic activity shown by the pre-activated compounds was hampered neither by loading nor H_2O_2 exposure time.

To further assess the chemical nature of **3** and **4**, the solids were examined by IR and Raman spectroscopy techniques. The typical four IR vibrational modes which determine the

https://doi.org/10.1021/acs.inorgchem.2c00342
Inorg. Chem. 2022, 61, 12494−12507

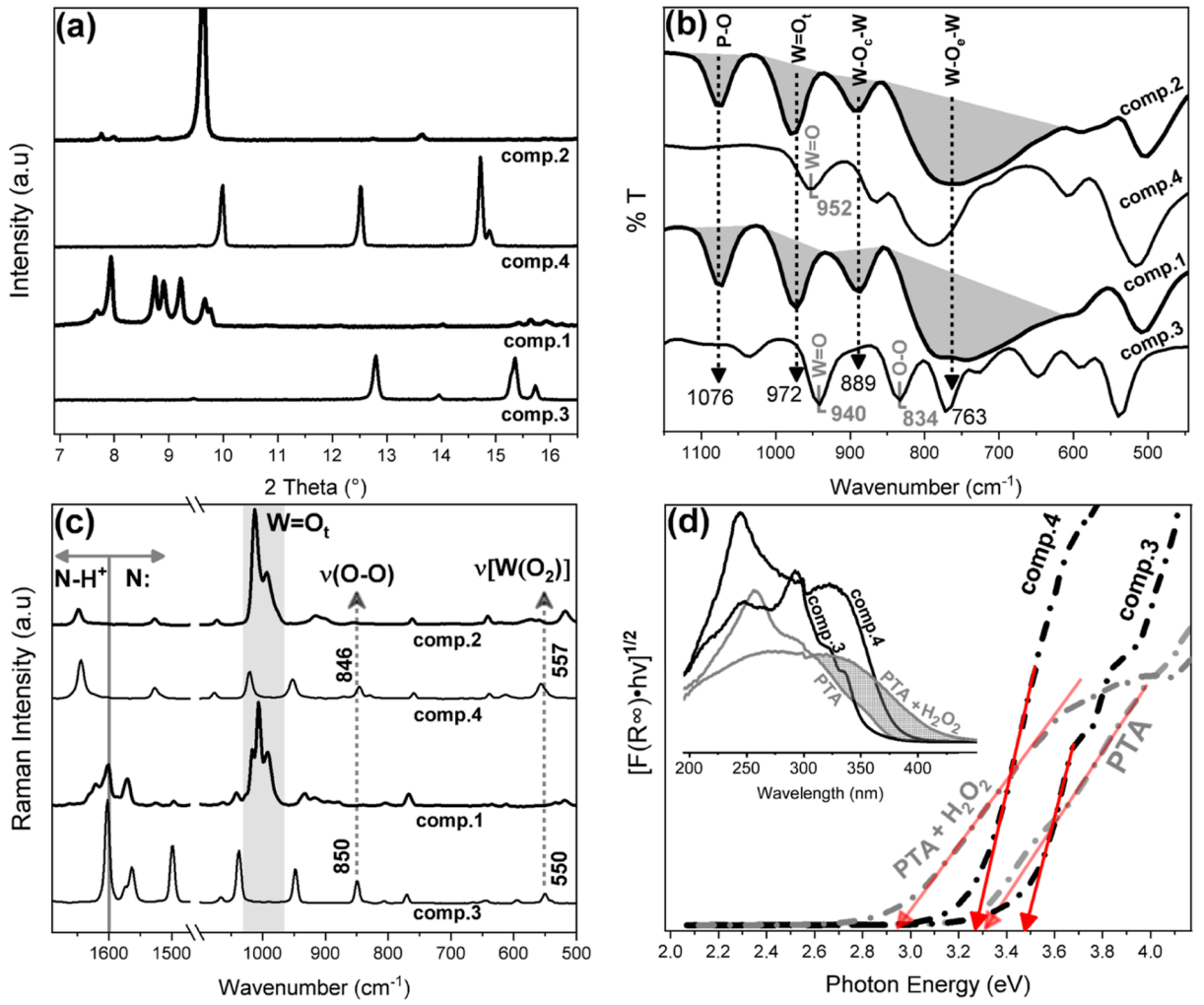

Figure 10. PXRD patterns (a) and IR (b) and Raman spectra (c) of compounds **1**, **2**, and pre-activated **3** and **4** ones. The Tauc's relation $[F(R_\infty)h\nu]^{1/2}$ *vs* photon energy (d) and Kubelka–Munk function *vs* wavelength [inset (d)] display PTA, PTA + H_2O_2, **3** and **4**.

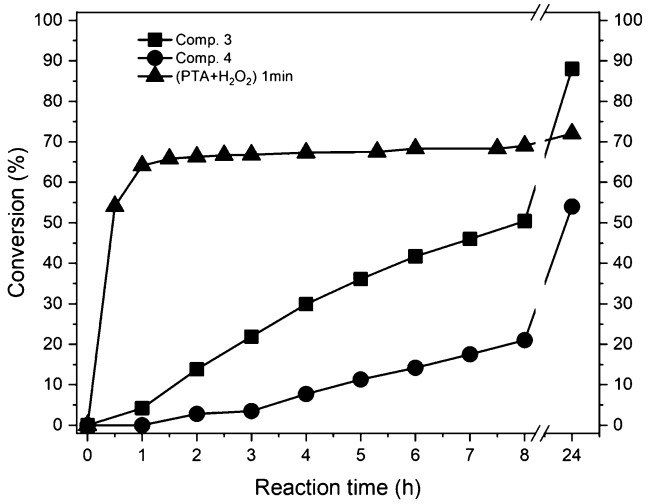

Figure 11. Epoxidation of cyclooctene catalyzed by pre-activated **3** and **4** compared to PTA. Reaction conditions: catalyst (0.02 mmol of W), H_2O_2 (1 mmol), cyclooctene (1 mmol), 70 °C.

presence of the POM structure as clearly displayed by **1** and **2**, are absent in **3** and **4** (Figure 10b). Instead, new bands occupied the low-frequency region showing stretching bands of W═O and O–O groups at 940 and 834 cm^{-1}, respectively, in **3**, whereas **4** only showed W═O (the O–O group is probably overlapped with the strong band centered at 790 cm^{-1}) at 952 cm^{-1}. Raman spectroscopy confirmed the POM structural loss of **3** and **4** as no band of W═O_t in the range of 1015–990 cm^{-1} was observed (Figure 10c).

Besides, new sets of bands at 850 and 550 cm^{-1} in **3** and 846 and 557 cm^{-1} in **4** attributed, respectively, to the vibration of O–O and W(O_2) groups confirm that **3** and **4** are composed of oxodiperoxotungstate species.[71] Interestingly, the ring stretching bands of 2,2′-bpy contained in **3**, appear at 1601 cm^{-1} and below, exhibiting an intermediate character between the protonated and neutral species. We suggest that the hybridized 2,2′-bpy is in a coordinative mode, as observed in earlier vibrational studies of 2,2′-bpy adsorbed on silica, alumina, zirconia, and titania.[72,73] On the other hand, the bands of 4,4′-bpy in **4** remain above 1600 cm^{-1} almost identical to that shown by **2**, suggesting that the ligand contained in **4** is a diprotonated 4,4′-bpyH_2^{2+} species. Based on these findings, it is reasonable to suggest that the epoxidation reaction with H_2O_2 catalyzed by **3** or **4** occurs *via* oxygen transfer from the corresponding peroxo complexes (Figure S5).

The absorption bands and E_g values of **3** and **4** were analyzed by DR–UV–vis (Figure 10d). PTA and PTA + H_2O_2

https://doi.org/10.1021/acs.inorgchem.2c00342
Inorg. Chem. 2022, 61, 12494–12507

were used as references in the interpretation of the spectra of **3** and **4**. The sample PTA + H_2O_2 was obtained by drying off the aqueous mixture (stirred for 1 h, ratio 1:100) overnight under vacuum at room temperature. The absorption band of PTA (3.3 eV) at 256 nm appears broader and less intense in the sample PTA + H_2O_2 (2.9 eV), whereas the lowest energy transition band of PTA (*ca.* 280−380 nm) is more intense in PTA + H_2O_2 and broadens toward higher wavelength (see the shaded area of the inset of Figure 10d). The decrease in absorption intensity of PTA was also observed by Aubry *et al.*[76] in the liquid state when PTA reacts with H_2O_2. This was attributed to the degradation of the Keggin polyanionic structure and formation of mixtures of less condensed (smaller anions) peroxo structures. However, interpretation of the band position and bandwidth of compounds derived from a degraded POM structure is not a trivial matter and definitive assignments are difficult to make. This is primarily due to the fact the degradation of the POM with H_2O_2 produces a panel of different peroxo complexes of various concentrations, atomic composition, anionic charge, and structures,[39,76] and therefore, the absorption bands can be influenced by a number of different effects. Nevertheless, a variety of well-defined peroxo complexes of molybdenum,[77] vanadium,[78−80] cobalt,[81] and peroxo groups attached to Keggin structures[82] have had unanimously their low energy transition band attributed to the peroxo-to-metal LMCT. Therefore, it is reasonable to assume that the marked shaded absorption area (*ca.* 308−450 nm) of the PTA + H_2O_2 sample corresponds to the electronic transitions of the peroxo species and is not related to the separation of the anionic units as above established for the structures of **1** and **2** (Figures 7 and 8). The absorption spectra of **3** (3.5 eV) and **4** (3.3 eV), on the other hand, show more intense and narrower absorption bands than PTA + H_2O_2. Both compounds show absorption bands at low wavelength centered at *ca.* 245 nm and bands in the peroxo region (*ca.* 278−400 nm). The former bands are presumably related to the electronic transition of the W═O groups (IR of Figure 10b) since PTA and some tungstate WO_4^{-2} salts[83] that contain W═O groups (without peroxo groups) also absorb in this high energy transition region. Compound **4** shows a broader absorption band than **3** toward high wavelength in the peroxo absorption region. A possible explanation of the different absorption energies of **3** and **4** is based on the assumption that the oxo O^{2-} (W═O) and peroxo O_2^{2-} (O−O) oxygens bonded to the tungsten atoms (which generate the $O^{2-} \rightarrow W^{6+}$ and $O_2^{2-} \rightarrow W^{6+}$ LMCT, respectively), are not in the same chemical environment. As observed in IR and Raman spectra(Figures 10b,c), the O−O, W═O, and W(O_2) bands of **3** and **4** do not vibrate at the same frequency. In addition, the interactions of bipyridine and the peroxo anions are not the same. The ligand 4,4′-bpy appears protonated, whereas 2,2′-bpy appears to be in a coordinative mode. Although definitive assignments of the exact chemical environment of the tungsten centers of the hybrids cannot be given by this technique,[56] it can be concluded that the absorption and corresponding E_g values of **3** and **4** are likely influenced by their local (oxygen-tungsten coordination sphere) and more distant (anionic interaction with bipyridine) chemical environments.

Finally, to investigate the chemical environment of the hybridized bipyridine ligands, the compounds were analyzed by liquid ^{1}H NMR (Figure 12). In this case, the liquid samples were obtained by filtering the suspension formed with CD_3CN. In the aromatic region (9.5−7.3 ppm), the neutral 2,2′-bpy

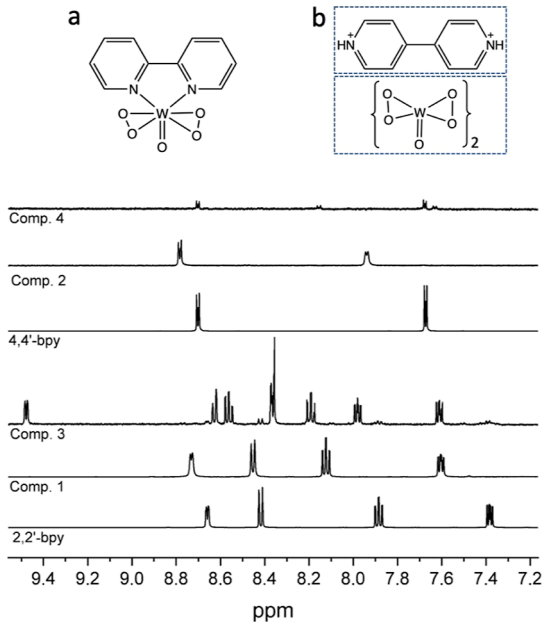

Figure 12. Liquid ^{1}H NMR spectra of compounds **1**−**4** and their respective neutral 2,2′-bpy and 4,4′-bpy precursors dissolved in CD_3CN. Inset (a) depicts a schematic representation of the presumed structure of compound **3** and inset (b) illustrates the structural components of **4**.

shows four resonance signals that correspond to the four protons of each equivalent pyridyl ring. Similarly, **1** displays the same four peaks but slightly shifted to higher ppm values. Compound **3**, on the other hand, shows eight resonance peaks. The increase of proton signals in **3**, relative to the neutral 2,2′-bpy, proves that 2,2′-bpy in **3** is coordinated to a tungsten atom.[74] The neutral 4,4′-bpy shows the two typical resonance signals in the aromatic region,[75] which are also present in **2** but shifted to higher ppm values. Compound **4**, however, exhibits two small signals centered at 8.7 and 7.7 ppm accompanied with two smaller peaks at 8.16 and 7.6 ppm. The two main peaks (8.7 and 7.7 ppm) correspond to trace amounts of 4,4′-bpy, whereas the two smaller ones are most likely the hybridized bipyridine in **4**. In all cases, the different integration ratio of the resonance signals is expected, as each compound solubilizes differently in CD_3CN.

In summary, NMR data confirm that bipyridine in **3** is coordinated to tungsten and that bipyridine in **4** is likely protonated. Upon protonation, the number of proton signals of bipyridine increases (*e.g.*, **3**), whereas the number of signals remains unchanged when protonated, as seen in the spectra of **1** and **2**. As a result, we suggest that the structure of **3** corresponds to a 2,2′-bipyridinium oxodiperoxotungstate complex (inset (a) of Figure 12). This is consistent with the atomic W/N ratio of **3** (W/2N = 0.5) calculated from the elemental analysis (Table 1). Compound **4**, on the other hand, is presumably composed of oxodiperoxotungstate {W(O_2)$_2$} moieties and diprotonated 4,4′-bpyH_2^{2+} species. Based on the calculated atomic W/N ratio of **4** equal to 0.5 (Table 1), **4** appears to be composed of one {W(O_2)$_2$} moiety per half of bipyridine, or two {W(O_2)$_2$} moieties per bipyridine (see inset (b) of Figure 12). As previously observed for the POM-based hybrids (*i.e.*, **1** and **2**), the isomerism of bipyridine also appears governing the number of ligands per anion (or tungsten center in the form of {W(O_2)$_2$}) for **3** and **4**. This,

https://doi.org/10.1021/acs.inorgchem.2c00342
Inorg. Chem. 2022, 61, 12494−12507

in turn, likely affected their catalytic performances in the epoxidation, even if occurring in the homogeneous phase. Despite being made of equivalent anionic $\{WO(O_2)_2\}$ moieties, the solubilities of **3** and **4** in the reaction mixture are likely to not be the same since the number of bipyridines per W atom in **3** is twice as high as that in **4**.

CONCLUSIONS

The present study has systematically examined the structural implications when selecting different isomers of bipyridine in the formation of Keggin POM-based hybrid materials. Their production can be efficiently achieved by combining commercial Keggin PTA and bipyridine sources hydrothermally. The physicochemical properties of the final material change dramatically depending on whether the isomer 2,2′-bpy or 4,4′-bpy is selected for hybridization. This was found to be a direct consequence of the acid−base properties of the ligands which, indeed, are determined by their conformational nature. Compound **1** appeared to be composed of 3 bipyridines per POM unit due to its stable ligand monoprotonated *cis*-2,2′-bpyH$^+$ form. The POM unit of compound **2**, on the other hand, appeared to be composed of half the amount of bipyridine of **1** and contained additional structural water. This is due to the unrestricted conformational nature of 4,4′-bpy prone to double protonate to 4,4′-bpyH$_2^{2+}$ species upon reaction with PTA. The observed ligand diminution led to inclusion of structural water in **2**, as **1** appeared to be hydrophobic enough to stay anhydrous. The hybridization showed to cause a structural distortion in the local octahedral units of hybridized POMs relative to the POM in PTA. Additionally, after hybridization, the distances between POM anions increased and thus lowered their reduction potentials. Exploiting this last feature, the compounds were tested as catalysts in the epoxidation of cyclooctene after having demonstrated the absence of remaining acid sites. The as-prepared **1** and **2** are poorly active since they are highly reluctant against degradation by H_2O_2. The cause is associated to the shielding effect exerted by the hydrophobic ligands on the hybridized POM, preventing it from engaging effectively with the hydrophilic oxidizing agent. Therefore, pre-degradation of the POM anion by H_2O_2 prior hybridization, leading to compounds **3** and **4**, is needed to induce the catalytic reaction. The pre-activated **3** and **4** displayed high activities and were highly selective. The structural composition of **3** and **4** showed that they were no longer composed of a POM structure but of oxodiperoxotungstate species which interact electrostatically with the isomer 4,4′-bpy (protonated) and in a coordinative mode with 2,2′-bpy. The different ligand/anion interactions, associated with the conformational nature of the isomers, were shown to unevenly change the chemical environment of the anion (*i.e.*, oxo O^{2-} (W═O) and peroxo O_2^{-2} (O−O) oxygens bonded to tungsten), and thus, their catalytic properties. The isomeric effect of bipyridine was shown to be of relevant importance in the catalytic performances of **3** and **4**. The number of bipyridines per W atom in **3** was twice as high as that in **4**, which seems to have affected their solubilities in the reaction mixture and, as a result, their concentration in the catalytic medium. Finally, the structural, bonding, and catalytic aspects covered here, are helpful to better rationalize when designing organic−inorganic hybrids based on bipyridine (or any other relative ligand) and Keggin POMs. This could open new avenues to produce sophisticated POM-based functional materials, with specific properties in a controllable and predictable manner, and extend to emerging application areas.

ASSOCIATED CONTENT

Supporting Information

The Supporting Information is available free of charge at https://pubs.acs.org/doi/10.1021/acs.inorgchem.2c00342.

PXRD patterns of fresh and exposed compounds **1** and **2**; IR spectra of exposed and fresh compounds **1** and **2**; Hot filtration tests of pre-activated **3** and **4**; Raman spectra of fresh and spent pre-activated **3** and **4**; and mechanism of the epoxidation reaction (PDF)

AUTHOR INFORMATION

Corresponding Author

Eric M. Gaigneaux − *Institute of Condensed Matter and Nanosciences (IMCN), Université Catholique de Louvain, 1348 Louvain-la-Neuve, Belgium;* orcid.org/0000-0003-2239-4306; Email: eric.gaigneaux@uclouvain.be

Authors

Gabriel Hidalgo − *Institute of Condensed Matter and Nanosciences (IMCN), Université Catholique de Louvain, 1348 Louvain-la-Neuve, Belgium;* orcid.org/0000-0001-5804-2850

Michel Devillers − *Institute of Condensed Matter and Nanosciences (IMCN), Université Catholique de Louvain, 1348 Louvain-la-Neuve, Belgium*

Complete contact information is available at: https://pubs.acs.org/10.1021/acs.inorgchem.2c00342

Notes

The authors declare no competing financial interest.

ACKNOWLEDGMENTS

Authors acknowledge the "Communauté française de Belgique" for the financial support through the ARC programme (15/20-069) and the purchase of the equipment thanks to F.N.R.S. (projects CDR J.0156.18 for DRUV and EQP U.N006.16 for PXRD).

REFERENCES

(1) Pope, M. T. *Heteropoly and Isopoly Oxometalates*; Springer, 1983; Vol. *8*.

(2) Zhang, S.-S.; Chen, J.-Y.; Li, K.; Yuan, J.-D.; Su, H.-F.; Wang, Z.; Kurmoo, M.; Li, Y.-Z.; Gao, Z.-Y.; Tung, C.-H.; Sun, D.; Zheng, L. Janus Cluster: Asymmetric Coverage of a Ag_{43} Cluster on the Symmetric Preyssler P_5W_{30} Polyoxometalate. *Chem. Mater.* **2021**, *33*, 9708−9714.

(3) He, H.; Wang, G.; Chai, S.; Li, X.; Zhai, L.; Wu, L.; Li, H. Self-Assembled Lamellar Nanochannels in Polyoxometalate-Polymer Nanocomposites for Proton Conduction. *Chin. Chem. Lett.* **2021**, *32*, 2013−2016.

(4) Zhao, Y.-Q.; Yu, K.; Wang, L.-W.; Wang, Y.; Wang, X.-P.; Sun, D. Anion-Induced Supramolecular Isomerism in Two Preyssler P_5W_{30} Polyoxometalate-Based Hybrid Materials. *Inorg. Chem.* **2014**, *53*, 11046−11050.

(5) Kozhevnikov, I. V. *Catalysis by Polyoxometalates*; Wiley, 2002; Vol. *2*.

(6) Hill, C. L. Introduction: PolyoxometalatesMulticomponent Molecular Vehicles To Probe Fundamental Issues and Practical Problems. *Chem. Rev.* **1998**, *98*, 1−2.

(7) Long, D. L.; Tsunashima, R.; Cronin, L. Polyoxometalates: Building Blocks for Functional Nanoscale Systems. *Angew. Chem., Int. Ed.* **2010**, *49*, 1736−1758.
(8) Misono, M. Catalysis of Heteropoly Compounds (Polyoxometalates). *Studies in Surface Science and Catalysis*; Elesivier; 2013, Chapter 4; Vol. *176*.
(9) Long, D. L.; Burkholder, E.; Cronin, L. Polyoxometalate Clusters, Nanostructures and Materials: From Self Assembly to Designer Materials and Devices. *Chem. Soc. Rev.* **2007**, *36*, 105−121.
(10) Proust, A.; Thouvenot, R.; Gouzerh, P. Functionalization of Polyoxometalates: Towards Advanced Applications in Catalysis and Materials Science. *Chem. Commun.* **2008**, 1837.
(11) Gómez-Romero, P.; Sanchez, C. *Functional Hybrid Materials*; Wiley, 2003.
(12) Maksimchuk, N. V.; Kovalenko, K. A.; Arzumanov, S. S.; Chesalov, Y. A.; Melgunov, M. S.; Stepanov, A. G.; Fedin, V. P.; Kholdeeva, O. A. Hybrid Polyoxotungstate/MlL-101 Materials: Synthesis, Characterization, and Catalysis of H_2O_2-Based Alkene Epoxidation. *Inorg. Chem.* **2010**, *49*, 2920−2930.
(13) Hao, X. L.; Ma, Y. Y.; Zang, H. Y.; Wang, Y. H.; Li, Y. G.; Wang, E. B. A Polyoxometalate-Encapsulating Cationic Metal-Organic Framework as a Heterogeneous Catalyst for Desulfurization. *Chem.—Eur. J.* **2015**, *21*, 3778−3784.
(14) Han, Q.; He, C.; Zhao, M.; Qi, B.; Niu, J.; Duan, C. Engineering Chiral Polyoxometalate Hybrid Metal-Organic Frameworks for Asymmetric Dihydroxylation of Olefins. *J. Am. Chem. Soc.* **2013**, *135*, 10186−10189.
(15) Haddadi, H.; Hafshejani, S. M.; Farsani, M. R.; Babahydari, A. K. Heterogeneous Epoxidation of Alkenes with H_2O_2 Catalyzed by a Recyclable Organic-Inorganic Polyoxometalate-Based Framework Catalyst. *New J. Chem.* **2015**, *39*, 9879−9885.
(16) Zhou, Y.; Guo, Z.; Hou, W.; Wang, Q.; Wang, J. Polyoxometalate-Based Phase Transfer Catalysis for Liquid-Solid Organic Reactions: A Review. *Catal. Sci. Technol.* **2015**, *5*, 4324−4335.
(17) Zou, C.; Zhang, Z.; Xu, X.; Gong, Q.; Li, J.; De Wu, C. A Multifunctional Organic-Inorganic Hybrid Structure Based on MnIII-Porphyrin and Polyoxometalate as a Highly Effective Dye Scavenger and Heterogenous Catalyst. *J. Am. Chem. Soc.* **2012**, *134*, 87−90.
(18) Sun, C. Y.; Liu, S. X.; Liang, D. D.; Shao, K. Z.; Ren, Y. H.; Su, Z. M. Highly Stable Crystalline Catalysts Based on a Microporous Metal−Organic Framework and Polyoxometalates. *J. Am. Chem. Soc.* **2009**, *131*, 1883−1888.
(19) Lian, L.; Zhang, H.; An, S.; Chen, W.; Song, Y.-F. Polyoxometalates-Based Heterogeneous Catalysts in Acid Catalysis. *Sci. China: Chem.* **2021**, *64*, 1117−1130.
(20) Orlandi, M.; Argazzi, R.; Sartorel, A.; Carraro, M.; Scorrano, G.; Bonchio, M.; Scandola, F. Ruthenium Polyoxometalate Water Splitting Catalyst: Very Fast Hole Scavenging from Photogenerated Oxidants. *Chem. Commun.* **2010**, *46*, 3152−3154.
(21) Puntoriero, F.; La Ganga, G.; Sartorel, A.; Carraro, M.; Scorrano, G.; Bonchio, M.; Campagna, S. Photo-Induced Water Oxidation with Tetra-Nuclear Ruthenium Sensitizer and Catalyst: A Unique 4 × 4 Ruthenium Interplay Triggering High Efficiency with Low-Energy Visible Light. *Chem. Commun.* **2010**, *46*, 4725−4727.
(22) Xiang, X.; Fielden, J.; Rodríguez-Córdoba, W.; Huang, Z.; Zhang, N.; Luo, Z.; Musaev, D. G.; Lian, T.; Hill, C. L. Electron Transfer Dynamics in Semiconductor-Chromophore-Polyoxometalate Catalyst Photoanodes. *J. Phys. Chem. C* **2013**, *117*, 918−926.
(23) Geletii, Y. V.; Botar, B.; Kögerler, P.; Hillesheim, D. A.; Musaev, D. G.; Hill, C. L. An All-Inorganic, Stable, and Highly Active Tetraruthenium Homogeneous Catalyst for Water Oxidation. *Angew. Chem., Int. Ed.* **2008**, *47*, 3896−3899.
(24) Zhang, Z.-M.; Zhang, T.; Wang, C.; Lin, Z.; Long, L.-S.; Lin, W. Photosensitizing Metal-Organic Framework Enabling Visible-Light-Driven Proton Reduction by a Wells-Dawson-Type Polyoxometalate. *J. Am. Chem. Soc.* **2015**, *137*, 3197−3200.
(25) Yu, X. Y.; Cui, X. B.; Lu, J.; Luo, Y. H.; Zhang, H.; Gao, W. P. Five Inorganic-Organic Hybrids Based on Keggin Polyanion $[SiMo_{12}O_{40}]^{4-}$: From 0D to 2D Network. *J. Solid State Chem.* **2014**, *209*, 97−104.
(26) Wang, J.-P.; Guo, G.-L.; Niu, J.-Y. Hydrothermal Syntheses, Crystal Structures of Three New Organic-Inorganic Hybrids Constructed from Keggin-Type $[BW_{12}O_{40}]^{5-}$ Clusters and Transition Metal Complexes. *J. Mol. Struct.* **2008**, *885*, 161−167.
(27) Xiao, L. N.; Wang, L. M.; Shan, X. N.; Guo, H. Y.; Fu, L. W.; Hu, Y. Y.; Cui, X. B.; Li, K. C.; Xu, J. Q. Secondary Organic Moiety Templated Organic-Inorganic Polyoxometalate-Based Frameworks. *CrystEngComm* **2015**, *17*, 1336−1347.
(28) Pang, H.; Peng, J.; Sha, J.; Tian, A.; Zhang, P.; Chen, Y.; Zhu, M. Syntheses of Two New Hybrid Compounds Based on Keggin Polyoxotungstates: The Use of Rigid and Flexible Ligands. *J. Mol. Struct.* **2009**, *922*, 88−92.
(29) Sha, J.; Peng, J.; Liu, H.; Chen, J.; Dong, B.; Tian, A.; Su, Z. Keggin POMs Modified by Bonding to Multitrack Cu(Bipy) Chains through Linearly Arrayed Terminal and Bridging Oxygen Atoms of the M_3O_{13} Triad. *Eur. J. Inorg. Chem.* **2007**, *2007*, 1268−1274.
(30) Yu, F.; Kong, X. J.; Zheng, Y. Y.; Ren, Y. P.; Long, L. S.; Huang, R. B.; Zheng, L. S. PH-Dependent Assembly of 0D to 3D Keggin-Based Coordination Polymers: Structures and Catalytic Properties. *J. Chem. Soc., Dalton Trans.* **2009**, 9503−9509.
(31) Fang, G.; Zhu, Y.; Du, C.; Hydrothermal Synthesis, S. L. Crystal Structure and Thermal Property of $(4,4'\text{-BipyH})_3[PW_{12}O_{40}]\cdot(4,4'\text{-Bipy})\cdot 7H_2O$. *J. Mol. Sci.* **2006**, *22*, 367−371.
(32) Yan, Q. X.; Shen, Y.; Niu, J. Y.; Wang, J. P. The Hydrothermal Synthesis and Crystal Structure of $[2.2'\text{-BipyH}]_3PW_{12}O_{40}$. *Russ. J. Inorg. Chem.* **2009**, *54*, 930−934.
(33) Wang, J.; Bi, D.; Niu, J. Hydrothermal Synthesis and Crystal Structure of a Tungstovanadate: $[4,4'\text{-BipyH}_2][4,4'\text{-BipyH}]_2[VW_{12}O_{40}]\cdot 4,4'\text{-Bipy}\cdot 7.5H_2O$. *Russ. J. Inorg. Chem.* **2009**, *54*, 403−406.
(34) Yang, M.-X.; Lin, S.; Chen, X.-H.; Luo, M.-H.; Liu, J.-H. Two organic-inorganic hybrid compounds constructed from 12-tungstovanadate and bipyridine. *J. Coord. Chem.* **2010**, *63*, 406−417.
(35) Li, Y. U.; Yuan, G. U. O.; Su, L. I. Hydrothermal Synthesis and Structural Characterization of Two Organic Inorganic Composite Heteropoly Compounds. *Chem. Res.* **2010**, *21*, 8−13.
(36) Liu, Y. B.; Wang, Y.; Xiao, L. N.; Hu, Y. Y.; Wang, L. M.; Cui, X. B.; Xu, J. Q. Two supramolecular structures constructed from Keggin-type polyoxometalates and 4,4′-bipyridine. *J. Coord. Chem.* **2012**, *65*, 4342−4352.
(37) Li, C. H.; Wang, Q.; Chi, Y. N.; Wang, X. F.; Hu, C. W. Supramolecular Assembly of Keggin Polyoxomolybdate and 2,2′-Bipyridine Generated in Situ from a Decarboxylation Coupling Reaction. *Chin. Chem. Lett.* **2013**, *24*, 578−580.
(38) Duncan, D. C.; Chambers, R. C.; Hecht, E.; Hill, C. L. Mechanism and Dynamics in the $H_3[PW_{12}O_{40}]$-Catalyzed Selective Epoxidation of Terminal Olefins by H_2O_2. Formation, Reactivity, and Stability of $\{PO_4[WO(O_2)_2]_4\}^{3-}$. *J. Am. Chem. Soc.* **1995**, *117*, 681−691.
(39) Salles, L.; Aubry, C.; Thouvenot, R.; Robert, F.; Doremieux-Morin, C.; Chottard, G.; Ledon, H.; Jeannin, Y.; Bregeault, J. M. ^{31}P and ^{183}W NMR Spectroscopic Evidence for Novel Peroxo Species in the "$H_3[PW_{12}O_{40}]\cdot yH_2O/H_2O_2$" System. Synthesis and X-Ray Structure of Tetrabutylammonium (μ-Hydrogen Phosphato)Bis(μ-Peroxo)Bis(Oxoperoxotungstate) (2-): A Catalyst of Olefin Epoxidation I. *Inorg. Chem.* **1994**, *33*, 871−878.
(40) Pazé, C.; Bordiga, S.; Zecchina, A. H_2O Interaction with Solid $H_3PW_{12}O_{40}$: An IR Study. *Langmuir* **2000**, *16*, 8139−8144.
(41) Moffat, J. B. *Metal-Oxygen Clusters*; Fundamental and Applied Catalysis; Springer US: Boston, MA, 2000.
(42) Barker, D. J.; Summers, L. A.; Cooney, R. P. Conformations of 2,2′-Bipyridine in Acidic Media. *J. Mol. Struct.* **1987**, *159*, 249−254.
(43) Moissette, A.; Batonneau, Y.; Brémard, C. Conformation and Protonation of 2,2′-Bipyridine and 4,4′-Bipyridine in Acidic Aqueous Media and Acidic ZSM-5 Zeolites: A Raman Scattering Study. *J. Am. Chem. Soc.* **2001**, *123*, 12325−12334.

https://doi.org/10.1021/acs.inorgchem.2c00342
Inorg. Chem. 2022, 61, 12494−12507

(44) Lu, T.; Cotton, T. M.; Birke, R. L.; Lombardi, J. R. Raman and surface-enhanced Raman spectroscopy of the three redox forms of 4,4'-bipyridine. *Langmuir* **1989**, *5*, 406−−414.
(45) Strukl, J. S.; Walter, J. L. Infrared and Raman Spectra of Heterocyclic Compounds-III. The Infrared Studies and Normal Vibrations of 2,2'-Bipyridine. *Spectrochim. Acta, Part A* **1971**, *27*, 209−221.
(46) Parker, L. M.; Bibby, D. M.; Burns, G. R. Fourier-Transform Infrared Study of Pyridine Sorbed on Zeolite HY. *J. Chem. Soc., Faraday Trans.* **1991**, *87*, 3319−3323.
(47) Cook, D. Vibrational Spectra of Pyridinium Salts. *Can. J. Chem.* **1961**, *39*, 2009−2024.
(48) Kamyshny, A. L.; Zakharov, V. N.; Fedorov, Y. V.; Galashin, A. E.; Aslanov, L. A. Surface-Enhanced Raman Scattering of 2,2′-Bipyridine Adsorbed on Colloidal Silver and Stabilized AgBr Sols. *J. Colloid Interface Sci.* **1993**, *158*, 171−182.
(49) Brolo, A. G.; Jiang, Z.; Irish, D. E. The orientation of 2,2′-bipyridine adsorbed at a SERS-active Au(111) electrode surface. *J. Electroanal. Chem.* **2003**, *547*, 163−172.
(50) Okuhara, T.; Mizuno, N.; Misono, M. Catalytic Chemistry of Heteropoly Compounds. *Adv. Catal.* **1996**, *41*, 113−252.
(51) Rocchiccioli-Deltcheff, C.; Thouvenot, R.; Franck, R. Spectres i.r. et Raman d'hétéropolyanions α-$XM_{12}O_{40}^{n-}$ de Structure de Type Keggin (X = B^{III}, Si^{IV}, Ge^{IV}, P^{V}, As^{V} et M = W^{VI} et Mo^{VI}). *Spectrochim. Acta, Part A* **1976**, *32*, 587−597.
(52) Arunan, E.; Desiraju, G. R.; Klein, R. A.; Sadlej, J.; Scheiner, S.; Alkorta, I.; Clary, D. C.; Crabtree, R. H.; Dannenberg, J. J.; Hobza, P.; Kjaergaard, H. G.; Legon, A. C.; Mennucci, B.; Nesbitt, D. J. Definition of the Hydrogen Bond (IUPAC Recommendations 2011). *Pure Appl. Chem.* **2011**, *83*, 1637−1641.
(53) Hardcastle, F. D.; Wachs, I. E. Determination of molybdenum-oxygen bond distances and bond orders by Raman spectroscopy. *J. Raman Spectrosc.* **1990**, *21*, 683−691.
(54) Altenau, J. J.; Pope, M. T.; Prados, R. A.; So, H. Models for Heteropoly Blues. Degrees of Valence Trapping in Vanadium(IV)- and Molybdenum(V)-Substituted Keggin Anions. *Inorg. Chem.* **1975**, *14*, 417−421.
(55) Varga, G. M.; Papaconstantinou, E.; Pope, M. T. Heteropoly blues. IV. Spectroscopic and magnetic properties of some reduced polytungstates. *Inorg. Chem.* **1970**, *9*, 662−667.
(56) Fournier, M.; Louis, C.; Che, M.; Chaquin, P.; Masure, D. Polyoxometallates as models for oxide catalysts Part I. An UV-visible reflectance study of polyoxomolybdates: Influence of polyhedra arrangement on the electronic transitions and comparison with supported molybdenum catalysts. *J. Catal.* **1989**, *119*, 400−414.
(57) Masure, D. Polyoxometallates as Models for Oxide Catalysts Part II. Theoretical Semi-Empirical Approach to the Influence of the Inner and Outer Mo Coordination Spheres on the Electronic Levels of Polyoxomolybdates. *J. Catal.* **1989**, *119*, 415−425.
(58) Tauc, J. Optical Properties and Electronic Structure of Amorphous Ge and Si. *Mater. Res. Bull.* **1968**, *3*, 37−46.
(59) Weber, R. S. Effect of Local Structure on the UV-Visible Absorption Edges of Molybdenum Oxide Clusters and Supported Molybdenum Oxides. *J. Catal.* **1995**, *151*, 470−474.
(60) Nomiya, K.; Sugie, Y.; Amimoto, K.; Miwa, M. Charge-Transfer Absorption Spectra of Some Tungsten(VI) and Molybdenum(VI) Polyoxoanions. *Polyhedron* **1987**, *6*, 519−524.
(61) Taketa, H.; Katsuki, S.; Eguchi, K.; Seiyama, T.; Yamazoe, N. Electronic Structure and Redox Mechanism of Dodecamolybdophosphate. *J. Phys. Chem.* **1986**, *90*, 2959−2962.
(62) Youn, M. H.; Kim, H.; Jung, J. C.; Song, I. K.; Barteau, K. P.; Barteau, M. A. UV−Vis Spectroscopy Studies of $H_3PMo_{12-x}W_xO_{40}$ Heteropolyacid (HPA) Catalysts in the Solid State: Effects of Water Content and Polyatom Substitution. *J. Mol. Catal. A: Chem.* **2005**, *241*, 227−232.
(63) Lee, J. K.; Melsheimer, J.; Berndt, S.; Mestl, G.; Schlögl, R.; Köhler, K. Transient Responses of the Local Electronic and Geometric Structures of Vanado-Molybdo-Phoshate Catalysts $H_{3+n}PV_nMo_{12-n}O_{40}$ in Selective Oxidation. *Appl. Catal., A* **2001**, *214*, 125−148.
(64) Kim, H.; Youn, M. H.; Jung, J. C.; Song, I. K. UV-Visible Absorption Edge Energy of Heteropolyacids (HPAs) as a Probe of Catalytic Performance of HPAs in the Oxidative Dehydrogenation of Isobutyric Acid. *J. Mol. Catal. A: Chem.* **2006**, *252*, 252−255.
(65) Sasca, V.; Popa, A. Band-Gap Energy of Heteropoly Compounds Containing Keggin Polyanion-$[PV_xMo_{12-x}O_{40}]^{-(3+x)}$ Relates to Counter-Cations and Temperature Studied by UV-VIS Diffuse Reflectance Spectroscopy. *J. Appl. Phys.* **2013**, *114*, 133503.
(66) Kozhevnikov, I. V. Catalysis by Heteropoly Acids and Multicomponent Polyoxometalates in Liquid-Phase Reactions. *Chem. Rev.* **1998**, *98*, 171−198.
(67) Essayem, N.; Coudurier, G.; Fournier, M.; Védrine, J. C. Acidic and Catalytic Properties of $Cs_xH_{3-x}PW_{12}O_{40}$ Heteropolyacid Compounds. *Catal. Lett.* **1995**, *34*, 223−235.
(68) Essayem, N.; Frety, R.; Coudurier, G.; Vedrine, J. C. Ammonia Adsorption-Desorption over the Strong Solid Acid Catalyst $H_3PW_{12}O_{40}$ and Its Cs^+ and NH_4^+ Salts Comparison with Sulfated Zirconia. *J. Chem. Soc., Faraday Trans.* **1997**, *93*, 3243−3248.
(69) Maeda, M.; Kato, K. Dissociation Constants of Ammonium Ion and Activity Coefficients of Ammonia in Ammonium Nitrate Solutions. *J. Chem. Eng. Data* **1995**, *40*, 253−256.
(70) Swalus, C.; Farin, B.; Gillard, F.; Devillers, M.; Gaigneaux, E. M. Hybrid Peroxotungstophosphate Organized Catalysts Highly Active and Selective in Alkene Epoxidation. *Catal. Commun.* **2013**, *37*, 80−84.
(71) Campbell, N. J.; Dengel, A. C.; Edwards, C. J.; Griffith, W. P. Studies on Transition Metal Peroxo Complexes. Part 8. The Nature of Peroxomolybdates and Peroxotungstates in Aqueous Solution. *J. Chem. Soc., Dalton Trans.* **1989**, 1203−1208.
(72) Bagshaw, S. A.; Cooney, R. P. FTIR and Raman spectroscopic investigation of 2, 2′-bipyridine adsorption on silica, alumina, zirconia and titania. *J. Mater. Chem.* **1994**, *4*, 557−563.
(73) Thornton, D. A.; Watkins, G. M. The Infrared Spectra (4000 - 50 cm^{-1}) of Complexes of Quinoline N-Oxide and Its Perdeuterated Analogue with Metal(II) Perchlorates of the First Transition Series. *J. Coord. Chem.* **1993**, *29*, 45−56.
(74) Baker, P. K.; Veale, P. L. 4,4′-Bipyridine Complexes of Molybdenum(II) and Tungsten(II). *Transition Met. Chem.* **2003**, *28*, 418−424.
(75) Gupta, G.; Kumar, J.; Garci, A.; Nagesh, N.; Therrien, B. Exploiting Natural Products to Build Metalla-Assemblies: The Anticancer Activity of Embelin-Derived Rh(III) and Ir(III) Metalla-Rectangles. *Molecules* **2014**, *19*, 6031−6046.
(76) Aubry, C.; Chottard, J. M.; Platzer, G.; Bregeault, R.; Thouvenot, N.; Chauveau, F.; Huet, C.; Ledon, H. Reinvestigation of Epoxidation Using Tungsten-Based Precursors and Hydrogen Peroxide in a Biphase Medium. *Inorg. Chem.* **1991**, *30*, 4409−4415.
(77) Bortolini, O.; Bragante, L.; Di Furia, F.; Modena, G. Metal Catalysis in Oxidation by Peroxides. 24. Extraction of Aqueous Peroxomolybdenum Species into Organic Media and Their Reactivity. *Can. J. Chem.* **1986**, *64*, 1189−1195.
(78) Bhattacharjee, M.; Chaudhuri, M. K.; Islam, N. S.; Paul, P. C. Synthesis, Characterisation and Physicochemical Properties of Peroxo-Vanadium(V) Complexes with Glycine as the Hetero-Ligand. *Inorg. Chim. Acta* **1990**, *169*, 97−100.
(79) Vennat, M.; Brégeault, J. M.; Herson, P. Mixed Crystals Containing the Dioxo Complex $[(Ph_3SiO)_2VO_2]^-$and Novel Pentacoordinated Oxoperoxo Complex $[(Ph_3SiO)_2VO(O_2)]^-$: X-Ray Crystal Structure and Assessment as Oxidation Catalysts. *J. Chem. Soc., Dalton Trans.* **2004**, 908−913.
(80) Gabriel, C.; Kaliva, M.; Venetis, J.; Baran, P.; Rodriguez-Escudero, I.; Voyiatzis, G.; Zervou, M.; Salifoglou, A. Aqueous V(V)-Peroxo-Amino Acid Chemistry. Synthesis, Structural and Spectroscopic Characterization of Unusual Ternary Dinuclear Tetraperoxo Vanadium(V)-Glycine Complexes. *Inorg. Chem.* **2009**, *48*, 476−487.
(81) Köferstein, R.; Robl, C. Synthesis Crystal Structure, and Hydrogen Bonding of μ-Hydroxo-μ-Peroxo-Bis[Bis-

https://doi.org/10.1021/acs.inorgchem.2c00342
Inorg. Chem. 2022, 61, 12494−12507

(Ethylenediamine)Cobalt(III)] Squarate. *Z. Anorg. Allg. Chem.* **2016**, *642*, 560−565.
(82) Yamase, T.; Ozeki, T.; Motomura, S. 183W NMR and X-Ray Crystallographic Studies on the Peroxo Complexes of the Ti-Substituted α-Keggin Typed Tungstophosphates. *Bull. Chem. Soc. Jpn.* **1992**, *65*, 1453−1459.
(83) Ross-Medgaarden, E. I.; Wachs, I. E. Structural Determination of Bulk and Surface Tungsten Oxides with UV−vis Diffuse Reflectance Spectroscopy and Raman Spectroscopy. *J. Phys. Chem. C* **2007**, *111*, 15089−15099.

https://doi.org/10.1021/acs.inorgchem.2c00342
Inorg. Chem. 2022, 61, 12494−12507